Electronic Supplementary Material (ESI) for CrystEngComm.

Supporting Information

From spent alkaline batteries to active Zn||$Zn_xMn_2O_4$ aqueous batteries: A mild process of cathode recycling and crystal engineering

Junjian Zhou,[a] Shen Wang,[a] Xinyu Wang,[a] Chengyu Zhang,[a] Zhengguo Gu,[a] Tong Zhou,[b] Zhiye Yuan,[b] Ting Long,[a] Jiang Yin,[a] Yahui Yang*[a] and Lishan Yang*[a]

a. *Key Laboratory of Chemical Biology & Traditional Chinese Medicine Research (Ministry of Education of China), National and Local Joint Engineering Laboratory for New Petrochemical Materials and Fine Utilization of Resources, Key Laboratory of the Assembly and Application of Organic Functional Molecules of Hunan Province, Hunan Normal University, Changsha, Hunan 410081, P. R. China.*

b. *Xiangtan Electrochemical Scientific Co., Ltd., Xiangtan, Hunan 411100, P. R. China.*

Corresponding authors: Tel./Fax.: +86 731 88872531

E-mail addresses:

yangyahui2002@sina.com (Y.H. Yang).

lsyang.chemistry@gmail.com (L.S. Yang)

Author Contributions：

Junjian Zhou: methodology, investigation, formal analysis, visualization and writing the original draft. Shen Wang: methodology, investigation, and data curation. Xinyu Wang: data curation. Chengyu Zhang: formal analysis. Zhengguo Gu: data curation. Zhengguo Gu, Tong Zhou, Zhiye Yuan and Ting Long: investigation. Jiang Yin: formal analysis, funding acquisition. Yahui Yang: visualization and funding acquisition. Lishan Yang: schematic design, supervision, conceptualization, formal analysis, writing - review & editing, funding acquisition. All authors reviewed the manuscript.

Preparation of recycled materials：

Spent NANFU alkaline batteries (ABs) were collected from the waste battery recycling bins, which were further discharged to 0.8 V with the Neware battery testing system (CT-4000) to completely release the remaining power. The cathode materials (of spent ABs) were collected, manually disintegrated, and denoted as spent materials (**SM**). In order to remove the residual binders and alkaline in SM, the SM powders were stirred in KOH solution (0.1M, AR, Sinopharm Chemical Reagent Co., Ltd.) for 15 minutes and washed with diluted H_2SO_4 solution (0.01 M). Finally, a brownish-black precipitate (recycled materials, **RM**) was obtained after being repeatedly washed (with deionized water and ethanol) and finally

dried in vacuum (60 °C).

Characterizations：

The structural information was recorded on an X-ray diffractometer (XRD， Bruker D8 advanced) with Cu Kα radiation (λ=1.5481 Å). The morphological and microstructural information was collected by using a scanning electron microscope (SEM, FEI Quanta FEG 250) and a transmission electron microscope (TEM, JEOL 2100). Scanning TEM testing was performed on an FEI Tecnai G2 TF20 to collect the energy-dispersive spectroscopy (EDS) elemental mapping results. The surface elemental properties of the samples were analyzed by using an X-ray photoelectron spectrometer (XPS, Thermo Fisher Scientific ESCALAB 250Xi) with Al Kα X-ray excitation source. The pH values were measured by Lichen pH-100B meter.

Electrochemical measurement：

According to a typical electrode fabrication method, SM (or RM) powders, acetylene black, and polyvinylidene fluoride (PVDF) were mixed with a mass ratio of 7:2:1 in N-methyl-2-pyrrolidone (NMP) and stirred uniformly. The homogeneous cathode slurry was pasted on a stainless-steel foil (0.01 mm) with a thickness of 50 μm and vacuum-baked at 80 °C for 12 hours for drying. A 2032-type coin cell was assembled with a Zn metal sheet as the counter electrode, a placing glass fiber (Whatman

Grade GF/D) as the separator, and the prepared cathode. “3 M $ZnSO_4$” and “3 M $ZnSO_4$ + 0.05 M $MnSO_4$” were used as two kinds of electrolytes in this work. The Neware battery test system was used to confirm the constant current charge and discharge performance under different conditions. The potential window was limited between 1.0 and 1.8 V vs. Zn/Zn^{2+}. Cyclic voltammetry (CV) and electrochemical impedance spectroscopy (EIS) analyses were performed on an electrochemical workstation (Ivium Vertex.C).

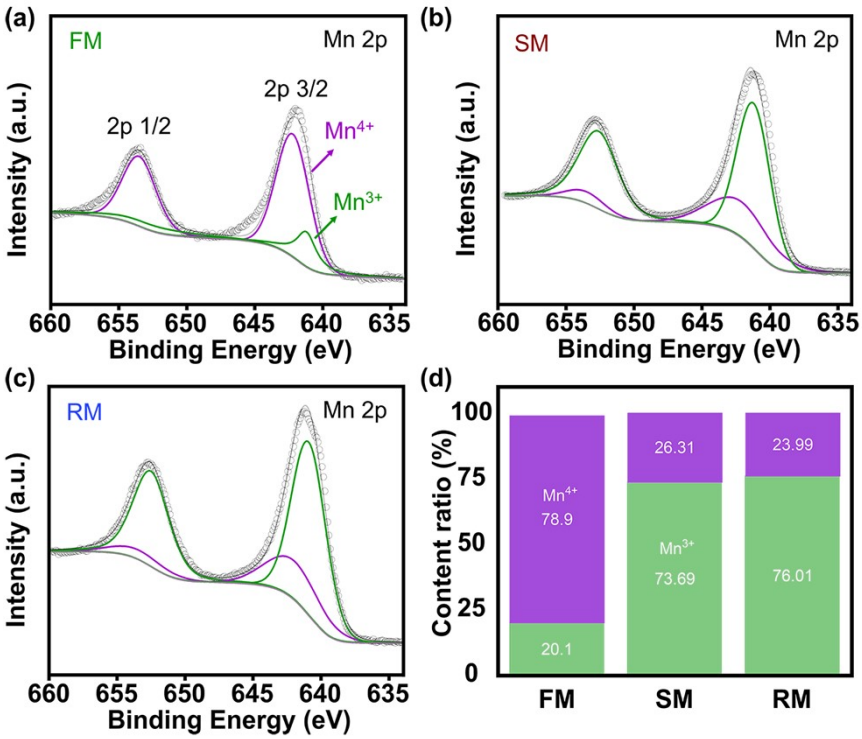

Fig. S1 The XPS patterns in Mn 2p region of (a)FM, (b)SM, (c)RM. (d) The content ratio of Mn^{3+} and Mn^{4+} in FM, SM, and RM.

Fig. S1 (a-c) reveal the existence of multiple Mn valences in FM, SM, and RM. The Mn^{3+} peak confirms the appearance of MnO(OH) in FM and exists in SM and RM. Mn^{4+} in both SM and RM demonstrates the formation of deficient spinel $Zn_xMn_2O_4$. The content ratio of Mn^{3+} and Mn^{4+} (Fig. S2d) shows the stability of the crystal in both SM and RM.

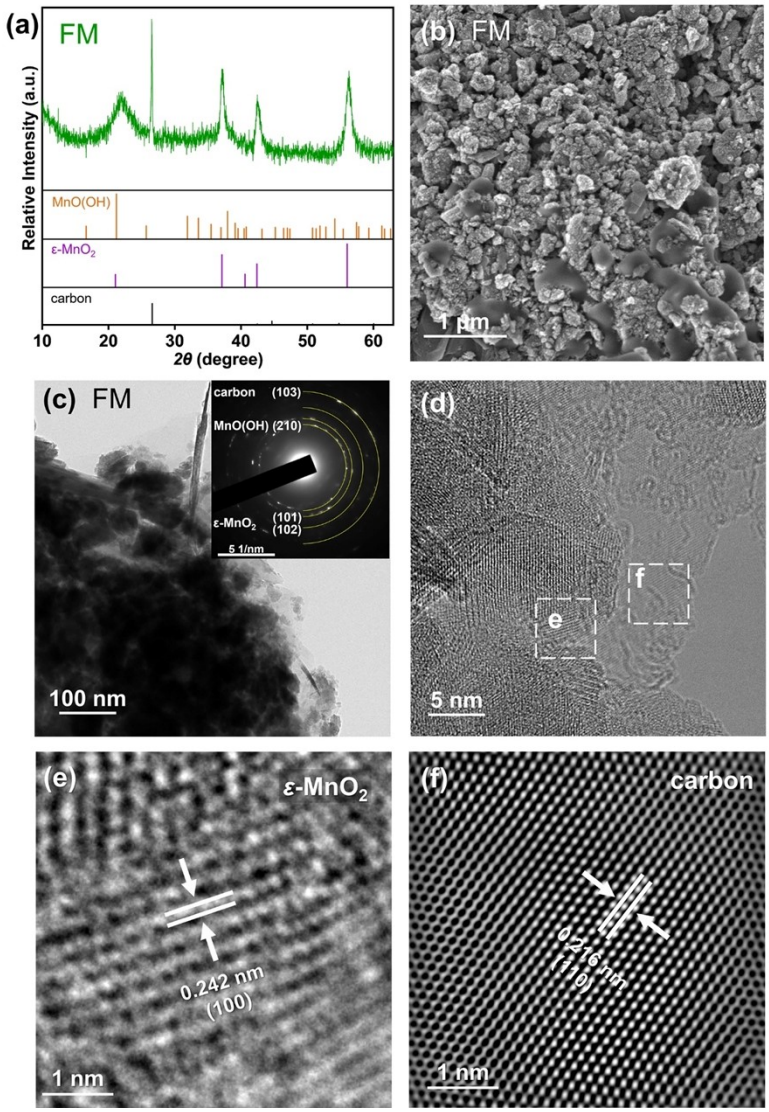

Fig. S2 The fresh cathode materials (FM) from a new alkaline battery without discharge: (a) XRD patterns, (b) a SEM image, (c) a TEM image and the corresponding SEAD pattern, (e, f) partially enlarged HRTEM images.

Fig. S2a shows that sample FM consists of MnO(OH) (JCPDS No. 88-0648), ε-MnO_2 (JCPDS No. 30-0820), and carbon (JCPDS No. 99-0057). The SEM image (Fig. S2b) demonstrates that sample FM is composed of many nano-aggregates and coral micro-particles. TEM, SEAD, and HRTEM (Fig. S2c-S2f) confirm the polycrystalline characters of FM materials.

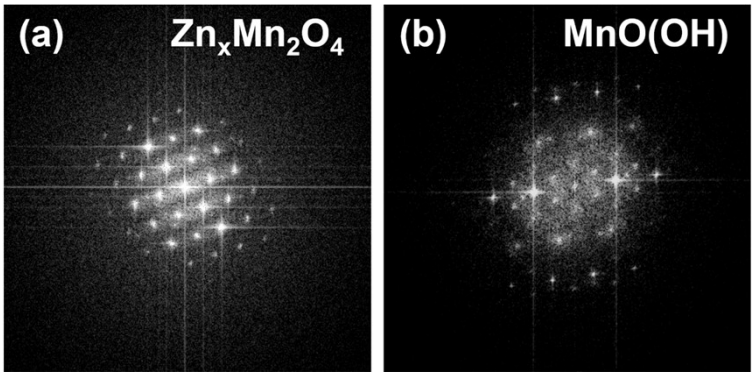

Fig. S3 The FFT pattern images of (a) $Zn_xMn_2O_4$ and (b) MnO(OH).

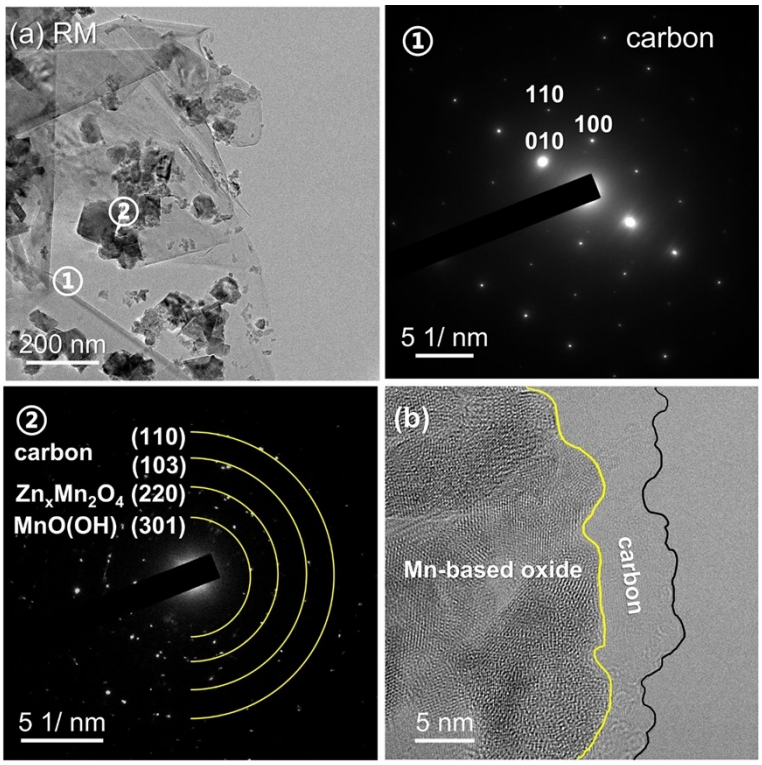

Fig. S4 The TEM image (a), SEAD (①, ②) and HRTEM (b) images of selected areas in (a) of RM powders.

In Fig. S4, TEM and HRTEM images of RM sample show that after post-treatment, the sample is a combination of crystalline $Zn_xMn_2O_4$, MnO(OH) particles and crystalline graphite films, and the amorphous substance in sample SM disappears.

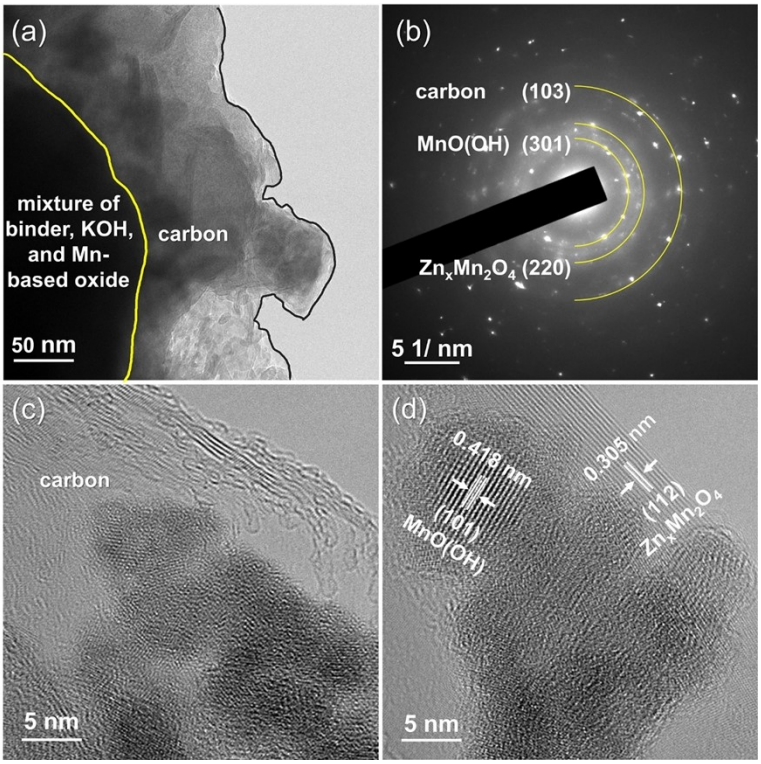

Fig. S5 The TEM (a), SEAD pattern (b), and HRTEM images (c and d) of sample SM.

The exposure of carbon in SM can be seen in Fig. S5a and Fig. S5c. The polycrystalline characters of SM are well-revealed by the clear diffraction rings (Fig. S5b) which show crystal planes (103) of carbon, (220) of $Zn_xMn_2O_4$, and (301) of MnO(OH). The lattice spacings of $Zn_xMn_2O_4$ (112) and MnO(OH) (101) planes are measured to be 0.305 nm and 0.418 nm respectively. Besides, there are many amorphous or weakly crystalline components in SM, which can also be observed in SAED and HRTEM images.

Table S1 The cycling performance comparison with various Zn_xMnO_4 cathodes.

Cathode	Electrolyte	Cycling performance	Current density	Ref.
RM	3 M $ZnSO_4$+0.05 M $MnSO_4$	251 mA h g^{-1} after 200 cycles	150 mA g^{-1}	This work
$ZnMn_2O_4/Mn_2O_3$	1 M $ZnSO_4$	119 mA h g^{-1} after 300 cycles	300 mA g^{-1}	1
Oxygen-extracted $ZnMn_2O_4$	1 M $ZnSO_4$	221 mA h g^{-1}	0.5 mA cm^2	2
$ZnMn_2O_4$ quantum dots@C	2 M $ZnSO_4$	200 mA h g^{-1} after 200 cycles	200 mA g^{-1}	3
Cation-defective $ZnMn_2O_4$/C	3 M $Zn(CF_3SO_3)_2$	150 mA h g^{-1} after 500 cycles	500 mA g^{-1}	4
Hollow porous spinel $ZnMn_2O_4$	1 M $ZnSO_4$+0.05 M $MnSO_4$	106.5 mA h g^{-1} after 300 cycles	100 mA g^{-1}	5
$ZnMn_2O_4$/N-doped graphene hybrid	1 M $ZnSO_4$+0.05 M $MnSO_4$	225 mA h g^{-1}	100 mA g^{-1}	6
$ZnMn_2O_4 \cdot 0.94H_2O$	1 M $ZnSO_4$+0.1 M $MnSO_4$	77 mA h g^{-1} after 2000 cycles	4000 mA g^{-1}	7
$ZnMn_2O_4$/CuO	2 M $ZnSO_4$+0.1 M $MnSO_4$	120 mA h g^{-1} after 100 cycles	300 mA g^{-1}	8
Mn_2O_3-$ZnMn_2O_4$ Hollow Heterostructures	2 M $Zn(CF_3SO_3)_2$+0.1 M $MnSO_4$	240.3 mA h g^{-1} after 80 cycles	100 mA g^{-1}	9
Mn Deficient $ZnMn_2O_4$@C Nanoarchitecture	2 M $ZnSO_4$+0.2 M $MnSO_4$	204 mA h g^{-1} after 70 cycles	300 mA g^{-1}	10

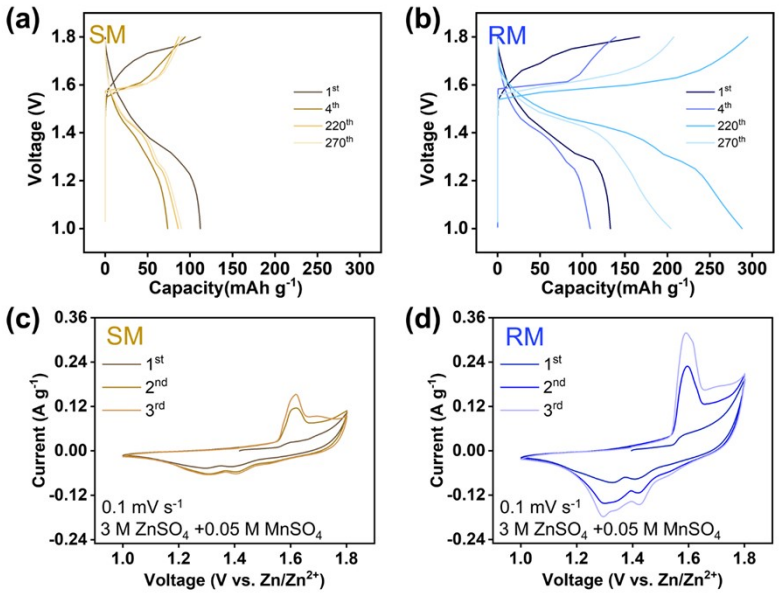

Fig. S6 The GCD curves for different cycles of SM and RM cathodes in Fig. 3a. The CV measurement of SM and RM in an electrolyte of 3 M $ZnSO_4$ with 0.05 M $MnSO_4$.

For the initial discharge curve, a more obvious plateau of Zn^{2+} insertion (~1.33 V) can be observed in RM cathode (Fig. S6b) rather than SM cathode (Fig. S6a). Based on the change of the two-stage discharge curve in Fig. S5b, the capacity increase of RM cathode before the 220th cycle could be contributed to both H^+ and Zn^{2+} intercalation s. After that cycle, the capacity of Zn^{2+} intercalation decreases more remarkably. Moreover, the area covered by the CV curves of RM, especially the reduction peak of Zn^{2+} intercalation near 1.3 V, increases significantly during the initial three cycles, which could be another proof of the capacity increase arisen mainly from Zn^{2+} insertion at the beginning.

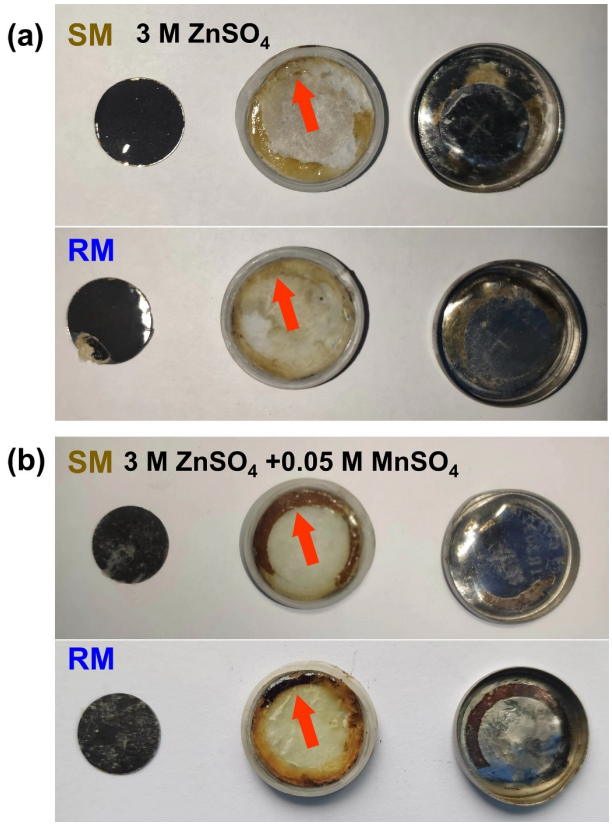

Fig. S7 (a) Images of disassembled SM and RM batteries after 200 cycles in the 3 M $ZnSO_4$ electrolyte. (b) Images of disassembled SM and RM batteries after 200 cycles in the 3 M $ZnSO_4$ + 0.05 M $MnSO_4$ electrolyte.

To further explore the causes of the capacity increase or decrease, we disassembled the coin cells after 200 cycles with different electrolytes between 1.0 and 1.8 V (vs. Zn/Zn^{2+}). Compared with a fresh separator, only a small amount of light brown marks appear at the edge of the separators of both cycled SM or RM batteries in the 3 M $ZnSO_4$ electrolyte (Fig. S7a). However, in the 3 M $ZnSO_4$ + 0.05 M $MnSO_4$ electrolyte, obvious brown ringed precipitations appear on both separators and cell shells of the cycled SM and RM batteries (Fig S7b). Combined with the later precipitates analysis and the electrochemical results under different

electrolytes, we can conclude that the cathodes will have obvious Mn^{2+} deposition and growth of Zn^{2+}-containing SEI film in $ZnSO_4$ + $MnSO_4$ hybrid electrolyte, which is similar to the previous reports.[11]

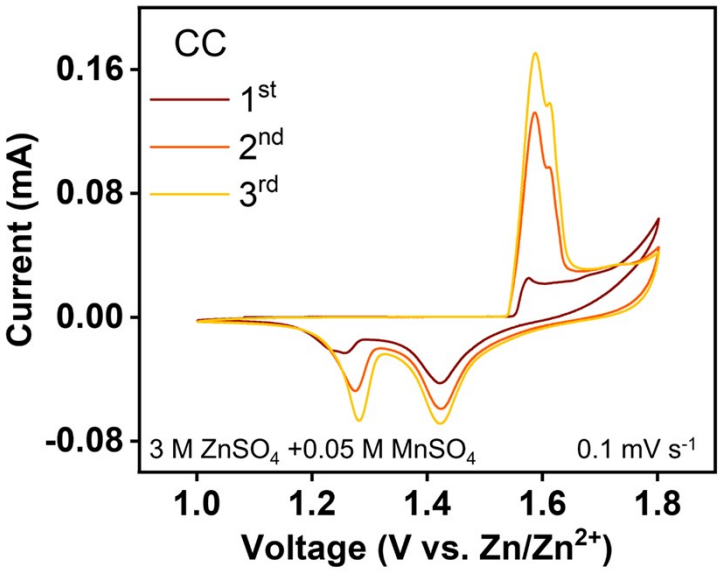

Fig. S8 The cathode-free CV measurement of a carbon cloth (CC) in 3 M $ZnSO_4$ with 0.05 M $MnSO_4$ electrolyte (under 0.1 mV s^{-1} between 1.0~1.8 V vs. Zn/Zn^{2+}).

Furthermore, the CV curves of a carbon cloth in 3 M $ZnSO_4$ with 0.05 M $MnSO_4$ prove that the manganese element of the deposition mostly comes from the electrolyte. As we can see, the first CV cycle has only one peak rather than two peaks in the next two cycles at about 1.6 V. But it has similar two peaks in cathodic scan at about 1.41 V and 1.25 V. This means the first cycle has a different reaction(s) at the oxidation sweep but has the same reaction(s) at the reduction sweep. This test began with a positive sweep which was used to obtain the evidence of manganese deposition excluding the possible influence of a negative sweep (such as hydrogen evolution or ion intercalation). So, the anodic scan at the first circle can be regarded as the manganese oxide (MnO_2) electrodeposited on the carbon cloth (CC). Because this is a one-step change, only one

characteristic peak appears.[12, 13] While at the cathodic scan in the first cycle, H^+ and Zn^{2+} co-inserted into manganese oxide, and then progressed to the second cycle.[14] Here, the peak at 1.25 V, which represents Zn^{2+} insertion, is also shifted to higher voltages when all peaks are enhanced from the first cycle to the third cycle. This phenomenon suggests that the ion intercalation/ deintercalation performance of freshly deposited manganese oxide has been enhanced (especially the Zn^{2+}). H^+ and Zn^{2+} can be completely extracted from discharge products (MnO(OH) and $Zn_xMn_2O_4$) during the negative sweep, which makes the CV peaks of manganese oxide at 1.6V more obvious. Specifically, those two different reactions are manifested as the appearance of two characteristic peaks.[15-17]

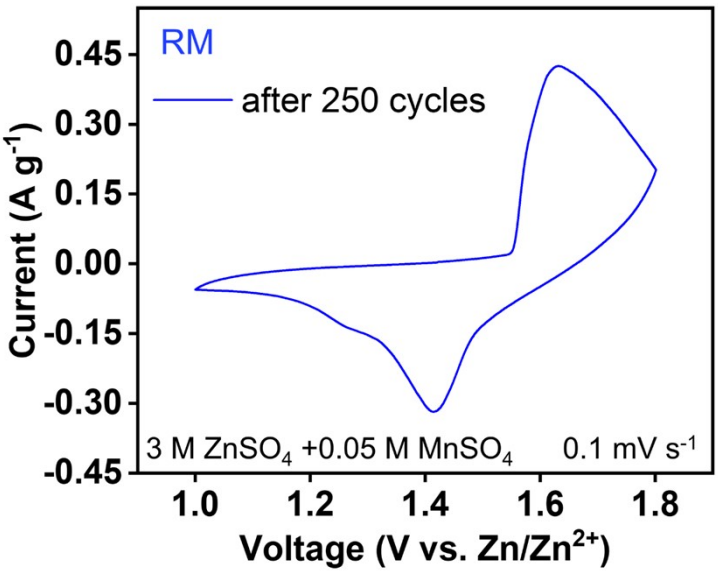

Fig. S9 The further CV measurement of RM battery after 250 cycles in 3 M $ZnSO_4$ with 0.05 M $MnSO_4$ electrolyte under 0.1 mV s^{-1}.

However, the CV curve after 250 cycles of RM shows that only the reduction peak of H^+ insertion was left, but the peak representing Zn^{2+} insertion was almost invisible, which is the reason for the capacity decay at the later stage of the cycling test.

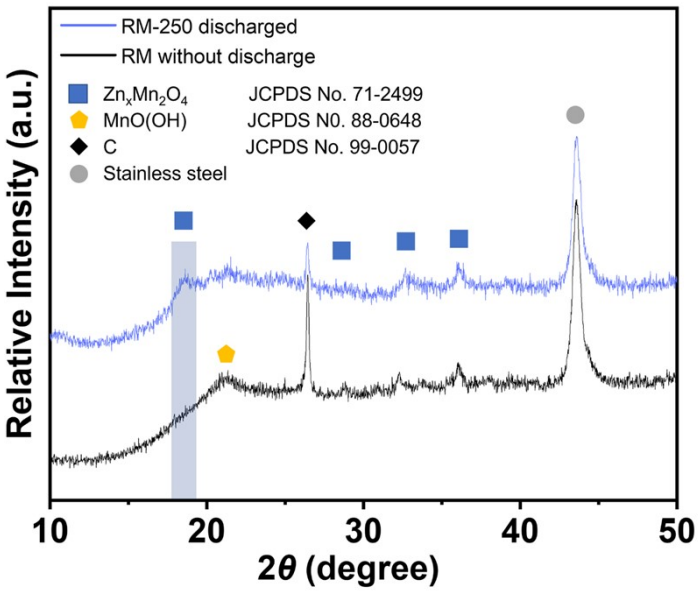

Fig. S10 XRD patterns of the RM cathode before (black) and after 250 cycles (blue, named as: RM-250) in the hybrid electrolyte (3 M $ZnSO_4$ + 0.05 M $MnSO_4$).

Compared with RM without discharge, a new peak belonging to $Zn_xMn_2O_4$ appears around 18.5°, while the carbon peak at 26.5° becomes weaker after 250 cycles. Combining the above results, it can be inferred that the new manganese oxide successfully coats the carbon surface and gradually transforms into $Zn_xMn_2O_4$, resulting in the capacity fading.

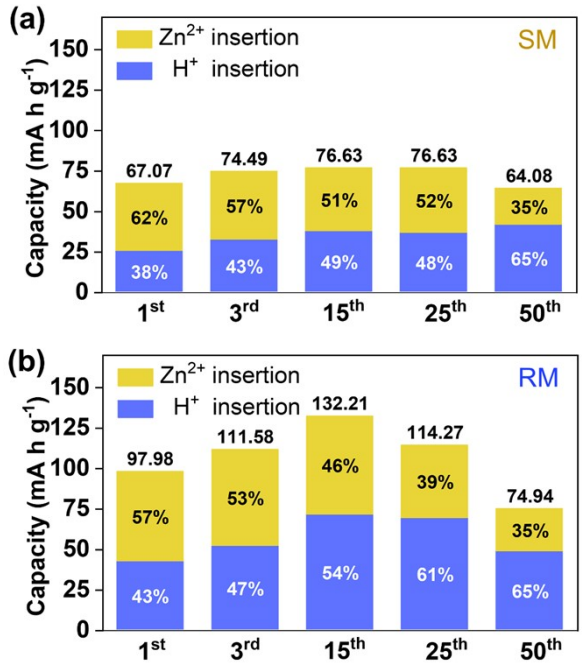

Fig. S11 The contribution of H^+ insertion and Zn^{2+} insertion in different cycles of SM (a) and RM (b) from Fig. 3c.

The insertion of H^+ at the high potential (above 1.4V) and the Zn^{2+} insertion at low potential (below 1.4 V). In SM (Fig. S11a), it seems that for most cycles, more than half of the capacity is contributed by Zn^{2+} insertion. However, in RM (Fig. S11b), the capacity provided by H^+ insertion increases rapidly and dominates after the 15th cycle. This result shows that the better capacity performance of RM is due to more H^+ insertions. Furthermore, at the 50th cycle, the capacities of both SM and RM are derived from H^+ insertion, which proves that the capacity drop is due to the hindered insertion of Zn^{2+}.

Fig. S12 The pH characterization of 2 mL 1 M $ZnSO_4$ electrolyte.

In Fig. 4a, the ratio of SM / RM sample and 3 M $ZnSO_4$ electrolyte was 0.07 g powder mixed with 2 mL liquid.

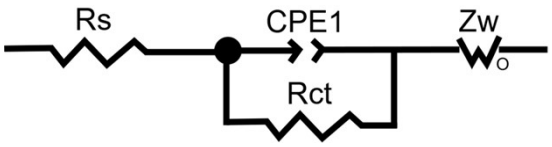

Fig. S13 The fitting model of SM and RM cathodes. An equivalent circuit (see inset) is used to simulate the resistances, where R_s, R_{ct}, CPE1, and W represent, respectively, the ohmic resistance of solution and electrodes, the charge-transfer resistance, constant phase angle element and the Warburg impedance.

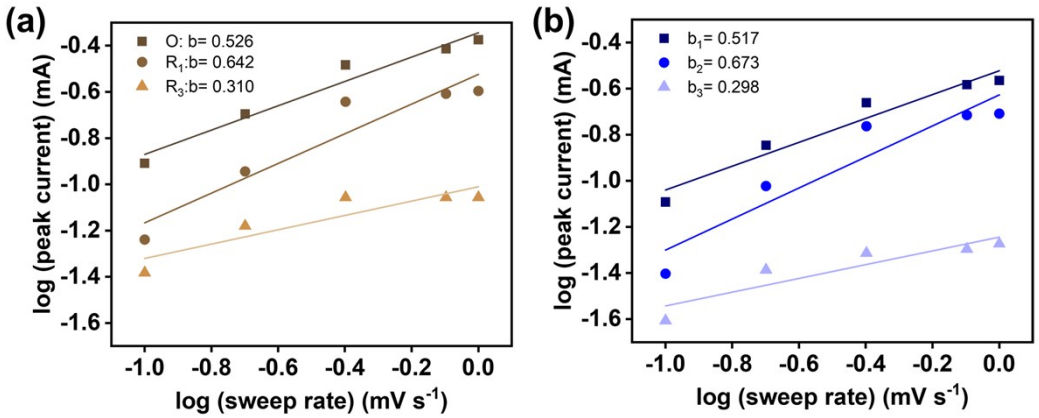

Fig. S14 Determination of the *b* values by using the relation between the peak current and scan rate for SM (a) and RM (b) cathodes.

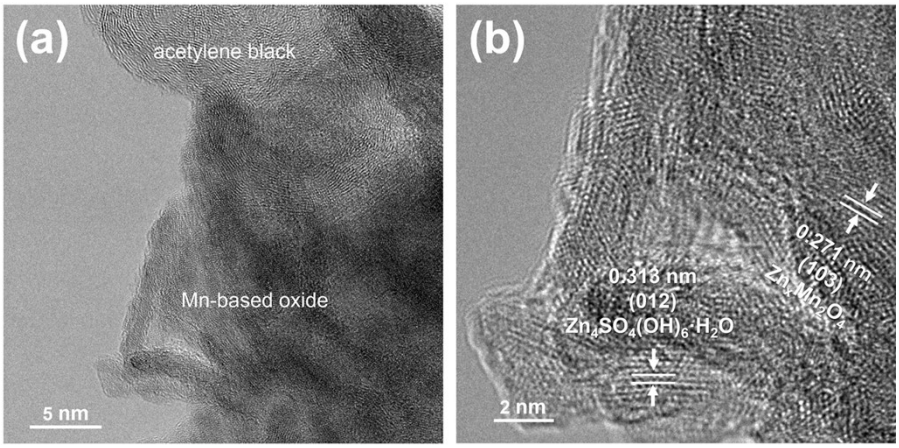

Fig. S15 The HRTEM images of the RM cathode after 50 cycles.

Compared with Fig. S4a, there is no exposed carbon could be found in Fig. S15a. The HRTEM images demonstrate that a mixture of $Zn_4SO_4(OH)_6 \cdot H_2O$ and $Zn_xMn_2O_4$ were formed in the discharged RM cathode.

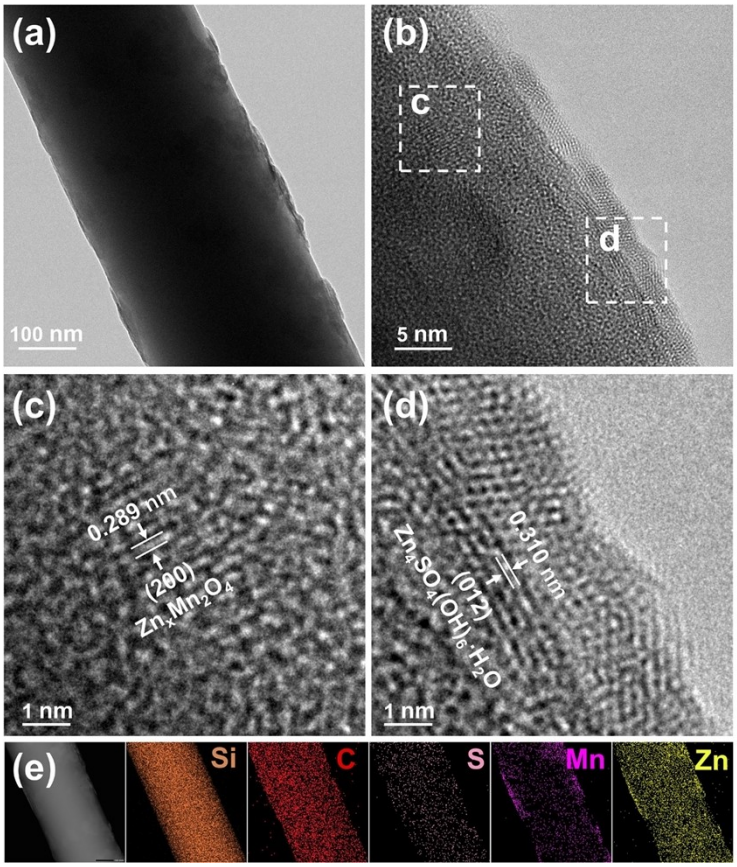

Fig. S16 TEM image (a), HRTEM image (b), and EDS elemental mapping (c) of the separator in RM coin cell after 50 cycles.

As Fig. S16a shows, the separator is woven of glass fiber. EDS elemental mapping (Fig. S16e) clearly shows that $Zn_xMn_2O_4$ and $Zn_4SO_4(OH)_6 \cdot H_2O$ can be found at the surface of SiO_x-C glass fibers.

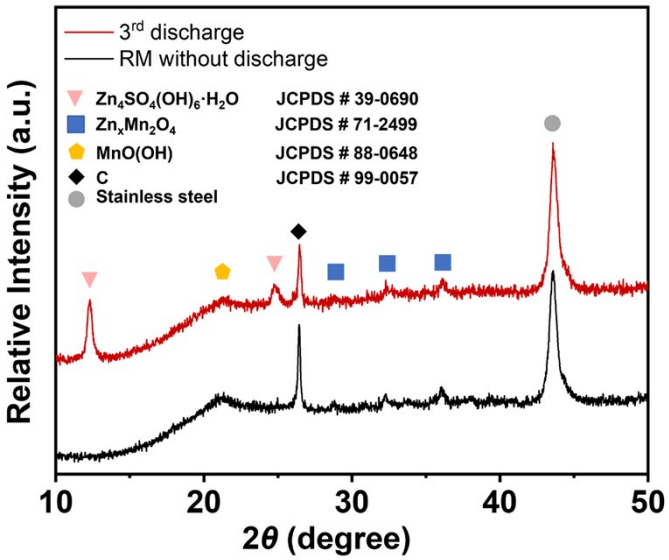

Fig. S17 XRD patterns of the RM cathode before (black) and after 3 cycles (red, named as: RM-3) in the hybrid electrolyte (3 M $ZnSO_4$ + 0.05 M $MnSO_4$).

Compared with the original RM cathode, two new peaks located at around 12.2° and 24.5° appear after three cycles (Fig.S17), both of which can be index to $Zn_4SO_4(OH)_6{\cdot}H_2O$ (JCPDS #39-0690). This result well proves our conjecture and corresponds well with the measurement results of TEM and EDS mapping (Fig.4, S15 and S16).

References：

1. S. Yang, M. Zhang, X. Wu, X. Wu, F. Zeng, Y. Li, S. Duan, D. Fan, Y. Yang and X. Wu, *J. Electroanal. Chem.*, 2019, **832**, 69-74.
2. H. Zhang, J. Wang, Q. Liu, W. He, Z. Lai, X. Zhang, M. Yu, Y. Tong and X. Lu, *Energy Storage Mater.*, 2019, **21**, 154-161.
3. S. Deng, Z. Tie, F. Yue, H. Cao, M. Yao and Z. Niu, *Angew. Chem. Int. Edit.*, 2022, **61**, e202115877.
4. N. Zhang, F. Cheng, Y. Liu, Q. Zhao, K. Lei, C. Chen, X. Liu and J. Chen, *J. Am. Chem. Soc.*, 2016, **138**, 12894-12901.
5. X. Wu, Y. Xiang, Q. Peng, X. Wu, Y. Li, F. Tang, R. Song, Z. Liu, Z. He and X. Wu, *J Mater. Chem. A*, 2017, **5**, 17990-17997.
6. L. Chen, Z. Yang, H. Qin, X. Zeng and J. Meng, *J. Power Sources*, 2019, **425**, 162-169.
7. T. Wu and W. Liang, *ACS Appl. Ma.Ter. Inter.*, 2021, **13**, 23822-23832.
8. L. Qin, Q. Zhu, L. Li, G. Fang, S. Li, H. Cheng, W. Guo and H. Gao, *Ionics*, 2021, **27**, 4783-4792.
9. Y. Zeng, Y. Wang, Q. Jin, Z. Pei, D. Luan, X. Zhang and X. W. Lou, *Angew. Chem. Int. Edit.*, 2021, **60**, 25793-25798.
10. S. Islam, M. H. Alfaruqi, D. Y. Putro, S. Park, S. Kim, S. Lee, M. S. Ahmed, V. Mathew, Y. K. Sun, J. Y. Hwang and J. Kim, *Adv. Sci. (Weinh.)*, 2021, **8**, 2002636.
11. N. Becknell, P. P. Lopes, T. Hatsukade, X. Zhou, Y. Liu, B. Fisher, D. Y. Chung, M. G. Kanatzidis, N. M. Markovic, S. Tepavcevic and V. R. Stamenkovic, *Adv. Funct. Mater.*, 2021, **31**, 2102135.
12. A. Dhiman and D. G. Ivey, *Batteries & Supercaps*, 2020, **3**, 293-305.
13. C. Xu, B. Li, H. Du and F. Kang, *Angew. Chem. Int. Edit.*, 2011, **51**, 933-935.
14. G. Sun, X. Jin, H. Yang, J. Gao and L. Qu, *J Mater. Chem. A*, 2018, **6**, 10926-10931.
15. Y. Li, S. Wang, J. R. Salvador, J. Wu, B. Liu, W. Yang, J. Yang, W. Zhang, J. Liu and J. Yang, *Chem. Mater.*, 2019, **31**, 2036-2047.
16. J. Yang, J. Cao, Y. Peng, W. Yang, S. Barg, Z. Liu, I. A. Kinloch, M. A. Bissett and R. A. W. Dryfe, *ChemSusChem*, 2020, **13**, 4103-4110.
17. Y. Huang, J. Mou, W. Liu, X. Wang, L. Dong, F. Kang and C. Xu, *Nanomicro Lett*, 2019, **11**, 49.